Alexandria Engineering Journal (2020) 59, 3515–3529

HOSTED BY

ELSEVIER

Alexandria University

Alexandria Engineering Journal

www.elsevier.com/locate/aej
www.sciencedirect.com

Effects of flexible fin on natural convection in enclosure partially-filled with porous medium

H. Saleh [a], **I. Hashim** [b,*], **E. Jamesahar** [c], **M. Ghalambaz** [d,e]

[a] *Mathematics Education Department, Universitas Islam Negeri Sultan Syarif Kasim Riau, 28293 Pekanbaru, Indonesia*
[b] *Department of Mathematical Sciences, Faculty of Science & Technology, Universiti Kebangsaan Malaysia, 43600 UKM Bangi Selangor, Malaysia*
[c] *Department of Mechanical Engineering, Dezful Branch, Islamic Azad University, Dezful, Iran*
[d] *Metamaterials for Mechanical, Biomechanical and Multiphysical Applications Research Group, Ton Duc Thang University, Ho Chi Minh City, Vietnam*
[e] *Faculty of Applied Sciences, Ton Duc Thang University, Ho Chi Minh City, Vietnam*

Received 11 February 2020; revised 27 April 2020; accepted 18 May 2020
Available online 6 July 2020

KEYWORDS

FSI;
Natural convection;
Porous media;
Brinkman-Forchheimer

Abstract A numerical study is conducted to analyze the effects of a flexible fin on unsteady convective flow in a square enclosure composed of a vertical fluid layer and a porous layer. The fin is attached to the heated left wall of the enclosure. The Brinkman-Forchheimer-extended Darcy flow model is assumed in the porous layer. The governing equations are written in the Arbitrary Lagrangian–Eulerian (ALE) formulation in the fluid and structure domains and then solved using the FEM. The result shows that the fin oscillation impacts the area below the fin rather than the area above the fin or the area in the center. The overall rate of heat transfer is improved as the Darcy number, the fluid layer thickness, and the fin elasticity increase. The overall rate of heat transfer increases exponentially with the rise of the oscillation amplitude. An oscillation amplitude of 0.1 could result in 3.4 percent improvement in the heat transfer rate.

1. Introduction

Convection in a differentially-heated porous-medium filled enclosure is an important problem in many engineering applications. Very often, the porous medium contains multilayer with different permeability or property, and the enclosure may be composed of a fluid layer and a porous layer. These composite systems have been applied in a widespread way, such as to remove or dissipate heat in electronics cooling applications [1]. Beckermann et al. [2] studied both numerically and experimentally natural convection in such a composite system. Later, Beckermann et al. [3] studied the enclosure fractionally loaded with the horizontal and vertical porous layer. They found that increasing the Darcy and Rayleigh numbers increased the amount of fluid action entering the porous layer. Du and Bilgen [4] and Song and Viskanta [5] studied both experimentally and theoretically convection in an enclosure containing an anisotropic porous layer. Chen and Chen [6]

* Corresponding author.
E-mail addresses: ishak_h@ukm.edu.my (I. Hashim), mohammad.ghalambaz@tdtu.edu.vn (M. Ghalambaz).
Peer review under responsibility of Faculty of Engineering, Alexandria University.

https://doi.org/10.1016/j.aej.2020.05.034

studied convection in an enclosure comprising a porous layer underlying a fluid layer. Convection of a binary fluid in an enclosure composed of a vertical porous layer and a fluid layer was studied by Goyeau et al. [7]. Chen et al. [8] placed a porous layer at the top and bottom parts of an enclosure and showed that the porous layer's thickness together with the Darcy number and the Rayleigh number could affect the heat transfer. Ismael and Chamkha [9] investigated convection in an enclosure composed of a vertical nanofluid layer and a nanofluid-filled porous layer. For different configurations, Baytas and Baytas [10] concluded that the governing equation has to obey the thermal non-equilibrium model for small values of the parameters. Recently, Alsabery et al. [11] reported that increasing the porous layer thickness could improve heat transfer. Sheikholeslami et al. [12] very recently studied nanoliquid natural convection through a permeable wavy space.

Alshuraiaan and Khanafer [13] examined the impact of a heated porous fin's location on convection heat transfer. The length of the fin was found by Sheikholeslami et al. [14] to have an inverse relationship with the discharging rate. Placing the rigid thin fin is categorized as a passive technique to increase heat transfer. Ghalambaz et al. [15] addressed the effect of actively oscillation fin, installed on the left hot side of the enclosure. They found a significant improvement in heat transfer enhancement by increasing the amplitude of the fin oscillation. This problem is classified under fluid–structure interaction (FSI) problems, and the Arbitrary Lagrangian–Eulerian (ALE) method is applied to solve it. Khanafer [16] explored the FSI of combined convective flow in a lid-driven enclosure filled with a clear fluid layer having a flexible bottom surface. The outcomes show that the elastic wall shape is affected by the convection intensity. Meanwhile, Khanafer [17] reported that the rate of heat transfer could be enhanced more by a non-rigid wall than a rigid wall. Selimefendigil and Oztop [18] showed that increasing the Richardson and Hartmann and internal Rayleigh numbers reduce the averaged heat transfer. Raising the flexibility of the wall and nanoparticle concentration enhances the heat transfer as found by Selimefendigil and Oztop [19]. Raisi and Arvin [20] considered an FSI problem where an adiabatic flexible baffle was placed at the center of an enclosure with a flexible top wall. They showed that increasing the baffle length has mixed effects on the thermal performance of the system. Alsabery et al. [21] revealed the essential effect of the flexible oscillating heat-conducting fin on the fluid flow and heat transfer inside the oblique enclosure. Alsabery et al. [22] considered the enclosure to have an inner solid cylinder and a flexible right wall. Ghalandari et al. [23] concluded that applying elastic solid structures with various sizes can bring to a significant modification in the system dynamics. Nonlinear identification of a narrow cantilever blade undergoing free vibration was studied by Mahariq et al. [24].

An FSI problem in a two-layered enclosure containing a flexible fin has not been studied before. In the present work, the influence of the fluid layer thickness, the amplitude, frequency oscillation, Darcy number, and the fin size on the convective heat transfer in the enclosure will be examined. A porous-fluid composite system having a flexible fin could be applied to the heat exchanger. Here the porous medium increases the contact surface area between the liquid and solid surface, and on the other hand, a flexible fin pulsates the flow in a forward or backward-facing step. Therefore it seems that using both a porous medium and a flexible fin can augment the efficiency of the typical thermal system dramatically.

2. Mathematical formulation

The problem geometry is presented in Fig. 1. The square enclosure consists of two layers: a fluid layer of width S^* and height H, and a porous layer of width $H - S^*$. A flexible structure (fin) with thickness b^* and length L^* is attached to the middle of the left wall. The tip of the flexible fin is forced to follow a sinusoidal vertical displacement as follows:

$$y^* = A^* \sin\left(\frac{2\pi t^*}{t_p^*}\right), \tag{1}$$

where y^* is the location of the fin tip, and t^* represents the time. t_p^* and A^* are the oscillation period and the oscillation amplitude, respectively. The fluid is Newtonian and incompressible, and the flow is laminar. Viscous dissipation, Joule heating and radiation were neglected. The porous medium is assumed to be homogeneous and isotropic. The gravity acts vertically downwards. All thermophysical properties of the fluid are invariant, except the density which obeys the Boussinesq approximation [25]. The fluid temperature variation is kept small, and the average fluid temperature is around the reference temperature.

The fin's deflection and heat conduction are modelled respectively as:

$$\rho_s \frac{d^2\mathbf{d}_s^*}{dt^{*2}} = \mathbf{F}_v^* + \nabla\boldsymbol{\sigma}^*, \tag{2}$$

$$\frac{\partial T^*}{\partial t^*} = \alpha_s \nabla^2 T^*. \tag{3}$$

Here $\mathbf{d}_s^*$ is the displacement vector, $\boldsymbol{\sigma}^*$ is stress tensor, T^* is the temperature and t^* is the time. Subscript s in the above-written equations refers to the structure. The structure's density is symbolized by ρ_s. The structure's thermal diffusivity is denoted by $\alpha_s = \frac{k_s}{\rho_s Cp_s}$, where k_s is the structure's conductivity and Cp_s is the structure's heat capacity. The symbol F_v^* represents the body force. Invoking the Arbitrary Lagrangian–Eulerian (ALE) system of moving mesh, the equations in the clear fluid layer are written as [15]:

$$\nabla \cdot \mathbf{u}^* = 0, \tag{4}$$

$$\frac{\partial \mathbf{u}^*}{\partial t^*} + (\mathbf{u}^* - \mathbf{w}^*) \cdot \nabla \mathbf{u}^* = -\frac{1}{\rho_f}\nabla P^* + \nu_f \nabla^2 \mathbf{u}^* + \beta \mathbf{g}\left(T^* - T_c^*\right), \tag{5}$$

$$\frac{\partial T^*}{\partial t^*} + (\mathbf{u}^* - \mathbf{w}^*) \cdot \nabla T^* = \alpha_f \nabla^2 T^*. \tag{6}$$

Here the symbol $\mathbf{u}^*$ represents the velocity vector in the clear fluid layer, $\boldsymbol{\sigma}^*$ denotes the stress tensor, and $\mathbf{d}_s^*$ is displacement vector of the solid. Here, E^* is Young's modulus. Symbol $\mathbf{w}^*$ denotes the moving mesh velocity. P^* is the pressure. Subscript f in the above-written equations refers to the fluid. The fluid's density is symbolized by ρ_f. The fluid's thermal diffusivity is denoted by $\alpha_f = \frac{k_f}{\rho_f Cp_f}$, ν_f is fluid's kinematic viscosity, where k_f is fluid's conductivity and Cp_f is fluid's heat capacity. $\mathbf{g} = (0, -g)$ represents the gravitational acceleration.

In the ALE method, the mesh in the Eulerian domain moves following the structure movement. However, the Eulerian velocities shall be independent of the mesh movement,

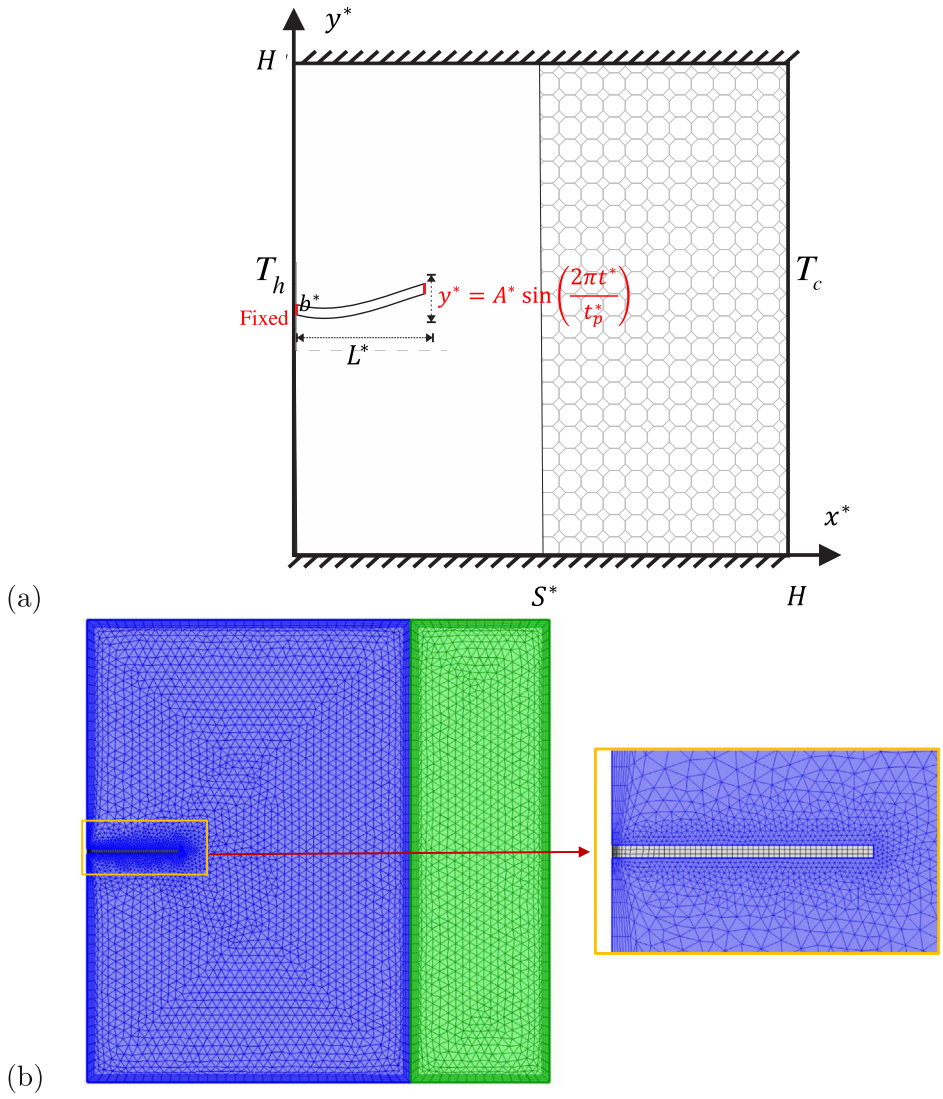

Fig. 1 (a) A schematic view of the model, (b) a picture of the mesh distribution.

and hence, the relative velocity terms $(\mathbf{u}^* - \mathbf{w}^*)$ are included in the governing equations. Hence, any arbitrary mesh movement is possible as the fluid velocities are introduced relative to the mesh movement, and eventually, the fluid velocity components are independent of the mesh velocity. The mesh velocity, $\mathbf{w}^*$ is controlled using a Laplace equation following the fluid–structure boundary displacements. Assuming the Brinkman-Forchheimer-extended Darcy flow model, the governing equations in the porous layer are [26]:

$$\nabla \cdot \mathbf{u}_p^* = 0, \tag{7}$$

$$\frac{1}{\epsilon}\frac{\partial \mathbf{u}_p^*}{\partial t^*} + \frac{1}{\epsilon^2}\mathbf{u}_p^* \cdot \nabla \mathbf{u}_p^* = -\frac{1}{\rho_f}\nabla P^* + \frac{\nu_f}{\epsilon}\nabla^2 \mathbf{u}_p^* + \beta \mathbf{g}\left(T_p^* - T_c^*\right) - \frac{\nu}{\kappa}\mathbf{u}_p^* - \frac{C_F}{\sqrt{\kappa}}\frac{|\mathbf{u}_p^*|}{\epsilon^{3/2}}\mathbf{u}_p^*, \tag{8}$$

$$\sigma\frac{\partial T_p^*}{\partial t^*} + \mathbf{u}_p^* \cdot \nabla T_p^* = \alpha_m \nabla^2 T_p^*. \tag{9}$$

Here T_p^* is the porous temperature. The symbols $\mathbf{u}_p^*$ is the porous velocity vector. The ratio of composite material heat capacity to convective fluid heat capacity is σ, ϵ is the porosity, κ is the permeability and $C_F = 1.75/\sqrt{150}$ is the Forchheimer constant [26]. The flexible segment has the hyperelastic property and based on the Winslow model, the stress tensor $\boldsymbol{\sigma}^*$ stated as:

$$\boldsymbol{\sigma}^* = \mathbf{J}^{-1}\mathbf{F}\mathbf{S}_{PK}\mathbf{F}^T, \tag{10}$$

where $\mathbf{J} = \det(\mathbf{F}), \mathbf{F} = \left(\mathbf{I} + \nabla \mathbf{d}_s^*\right)$, the second Piola–Kirchhoff stress tensor $\mathbf{S}_{PK} = \mathbf{C} : (\boldsymbol{\varepsilon})$ with strain $\boldsymbol{\varepsilon} = 0.5\left(\nabla \mathbf{d}_s^* + \mathbf{d}_s^{*T} + \mathbf{d}_s^{*T}\nabla \mathbf{d}_s^*\right)$ and $\mathbf{C} = \mathbf{C}(\mathbf{E}^*, \nu)$, where the nonlinear geometry effects are also taken into account. The fluid and structure are coupled through the boundary interface between the fluid and the structure as the velocity of the structure and the fluid are identical at the interface surface. The surface tensions are also identical at the interface. By incorporating the conventional no-slip at the fin surface, the interface boundary conditions are

$$\frac{\partial \mathbf{d}_s^*}{\partial t^*} = \mathbf{u}^* \quad \text{and} \quad \boldsymbol{\sigma}^* \cdot \mathbf{n} = -P^* + \mu_f \nabla \cdot \mathbf{u}^*. \tag{11}$$

Here μ_f is the dynamic viscosity. The term $\nabla \cdot \mathbf{u}^* = 0$ is the continuity equation for incompressible flow, and hence, it is

zero in the present study. This term shows the pressure at the surface due to the interaction of the fluid and fin. The boundary conditions at the interface are:

$$u^* = u_p^*,\ v^* = v_p^*, \tag{12}$$

$$\mu_f \frac{\partial u^*}{\partial n} = \mu_r \frac{\partial u_p^*}{\partial n},\ \mu_f \frac{\partial v^*}{\partial n} = \mu_r \frac{\partial v_p^*}{\partial n}, \tag{13}$$

$$k_f \frac{\partial T^*}{\partial n} = k_r \frac{\partial T_p^*}{\partial n}. \tag{14}$$

Here μ_r is the effective dynamic viscosity defined as $\mu_r = \epsilon\mu_f + (1-\epsilon)\mu_s$ and k_r is the effective thermal conductivity defined as $k_r = \epsilon k_f + (1-\epsilon)k_s$.

In the momentum equation, the pressure term appears in the form of the pressure gradient (∇P^*). Hence, the pressure differences are important in the momentum equation rather than the absolute pressure. When the momentum equations along with the continuity equation are solved, a pressure gradient satisfying the governing equations will be obtained. The pressure gradient in the form of the Laplace equation can be solved for the pressure field. The zero pressure reference is selected at the enclosure's bottom left corner.

Taking dimensionless parameters

$$d_s = \tfrac{d_s^*}{L^*},\ (A,L,b) = \tfrac{(A^*,L^*,b^*)}{H},\ \sigma = \tfrac{\sigma^*}{E^*},\ (x,y) = \tfrac{(x^*,y^*)}{H},$$
$$t = \tfrac{t^*\alpha_f}{H^2},\ \mathbf{u} = \tfrac{H\mathbf{u}^*}{\alpha_f},\ \mathbf{u_p} = \tfrac{H\mathbf{u}_\mathbf{p}^*}{\alpha_m},\ \mathbf{w} = \tfrac{H\mathbf{w}^*}{\alpha_f},\ P = \tfrac{P^*H^2}{\rho_f\alpha_f^2},\ T = \tfrac{T^*-T_c}{T_h-T_c}, \tag{15}$$

$$Ra = \frac{g\beta(T_h - T_c)H^3}{\nu_f\alpha_f},\ Pr = \frac{\nu_f}{\alpha_f},\ \rho_r = \frac{\rho_s}{\rho_f},\ Da = \frac{\kappa}{H^2},$$

yields the following dimensionless equations

$$\frac{1}{\rho_r}\frac{d^2 d_s}{dt^2} - E\nabla\sigma = EF_v, \tag{16}$$

$$\frac{\partial T}{\partial t} = \alpha_r \nabla^2 T, \tag{17}$$

$$\nabla\cdot\mathbf{u} = 0, \tag{18}$$

$$\frac{\partial \mathbf{u}}{\partial t} + (\mathbf{u}-\mathbf{w})\cdot\nabla\mathbf{u} = -\nabla P + Pr\nabla^2\mathbf{u} + Pr\,Ra\,T, \tag{19}$$

$$\frac{\partial T}{\partial t} + (\mathbf{u}-\mathbf{w})\cdot\nabla T = \nabla^2 T, \tag{20}$$

$$\nabla\cdot\mathbf{u}_p = 0, \tag{21}$$

$$\tfrac{1}{\epsilon}\tfrac{\partial \mathbf{u_p}}{\partial t} + \tfrac{1}{\epsilon^2}\mathbf{u}_p\cdot\nabla\mathbf{u}_p = -\nabla P + \tfrac{Pr}{\epsilon}\nabla^2\mathbf{u}_p + Ra\,Pr\,T_p - \tfrac{Pr}{Da}\mathbf{u}_p, \quad - \tfrac{C_F}{\sqrt{Da}}\tfrac{|\mathbf{u}_p|}{\epsilon^{3/2}}\mathbf{u}_p, \tag{22}$$

$$\sigma_m\frac{\partial T_p}{\partial t} + \mathbf{u}_p\cdot\nabla T_p = R_k\nabla^2 T_p^*. \tag{23}$$

Here R_k is the ratio of thermal conductivities defined as $R_k = k_r/k_f$. The initial velocity and temperature are set 0 and 0.5, respectively. The appropriate conditions on temperature are:

$$T = 1(\text{left wall}),\ T = 0(\text{right wall}), \tag{24}$$

$$u = u_p,\ v = v_p,\ \mu_f\frac{\partial u}{\partial n} = \mu_r\frac{\partial u_p}{\partial n},\ \mu_f\frac{\partial v}{\partial n} = \mu_r\frac{\partial v_p}{\partial n},$$
$$\frac{\partial T}{\partial n} = k_r\frac{\partial T_p}{\partial n}(\text{interface}). \tag{25}$$

The boundary conditions on the walls and the FSI interface are:

$$\frac{\partial \mathbf{d}_s}{\partial t} = \mathbf{u} \quad \text{and} \quad E\boldsymbol{\sigma}\cdot\mathbf{n} = -P + Pr\nabla\cdot\mathbf{u}. \tag{26}$$

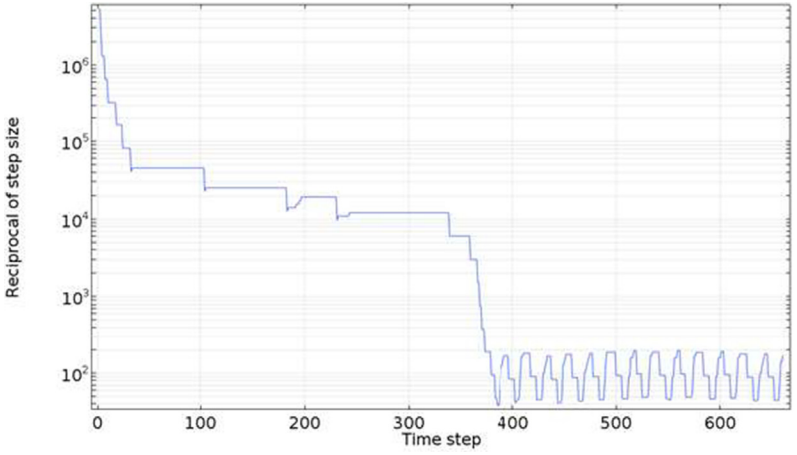

Fig. 2 The reciprocal of the time step size at $L = 0.2$, $E = 10^9$, $A = 0.1$, $Da = 10^{-3}$, $Ra = 10^7$, $S = 0.7$ $L = 0.2, E = 10^9, A = 0.1, Da = 10^{-3}, Ra = 10^7, S = 0.7$ and $t_p = 0.5$.

Table 1 Grid sensitivity checks at point $(x = 0.15, y = 0.8)$ with $L = 0.2$, $E = 10^9$ $A = 0.1$, $Da = 10^{-3}$, $Ra = 10^7$, $S = 0.7$ and $t_p = 0.5$.

Predefined mesh size	Domain elements	Boundary elements	$T_{t=0.01}$	$\lvert\text{Error}\rvert_{t=0.01}$	$T_{t=1.1}$	$\lvert\text{Error}\rvert_{t=1.1}$
Normal	2434	186	0.7373	0.0076	0.8953	0.0247
Fine	3067	216	0.7324	0.0125	0.8991	0.0209
Finer	4524	264	0.7378	0.0071	0.9035	0.0165
Extra fine	10220	388	0.7434	0.0015	0.9102	0.0098
Extremely fine	31861	646	0.7450	0.0001	0.9172	0.0028

The fin-tip displacement in dimensionless form is

$$y = A\sin\left(\frac{2\pi t}{t_p}\right). \tag{27}$$

The local Nusselt numbers at the heated wall and fin base are

$$Nu_{local,f}(t) = -\frac{\partial T(t)}{\partial x}\ \text{(heated wall)}, \tag{28}$$

$$Nu_{local,s}(t) = -k_r\frac{\partial T(t)}{\partial x}\ \text{(fin base)}. \tag{29}$$

Hence, the total average Nusselt number is

$$\overline{Nu}(t) = \int_0^{\frac{1-b}{2}} Nu_{local,f}(t)\mathrm{d}y + \int_{\frac{1-b}{2}}^{\frac{1+b}{2}} Nu_{local,s}(t)\mathrm{d}y + \int_{\frac{1+b}{2}}^{1} Nu_{local,f}(t)\mathrm{d}y, \tag{30}$$

and the time-averaged Nusselt number is

$$\overline{Nu} = \int_1^{1+5t_p} \overline{Nu}(t)\mathrm{d}t. \tag{31}$$

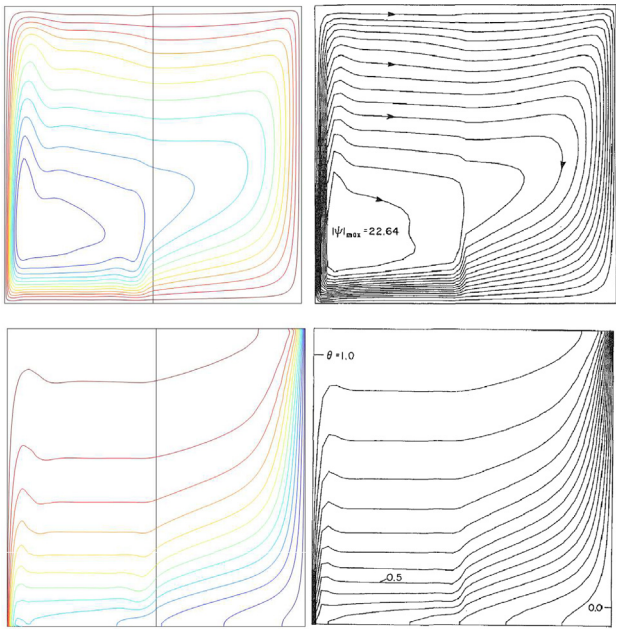

Fig. 3 Comparison of the present computed streamlines and isotherms (left) against that of literature (right) without the fin at $Ra = 3.028\times10^7$, $Da = 1.296\times10^{-5}$, $Pr = 6.97$, $R_k = 1.383$ and $S = 0.5$.

The fin oscillations reach to a semi steady-state at $t \approx 1$. After the steady-state, an interval of five oscillation-cycles, i.e. $(1 + 5t_p)$, is adopted for computation of time-averaged Nusselt number.

3. Numerical method

There are several approaches that can be adopted to solve the partial differential equations, such as the spectral element method [27–29] and finite volume method. However, here the Finite Element Method (FEM) is employed to solve the dimensionless governing equations. First, the flow equations are converted into the weak form. The domain solution is divided into non-overlapping regions, with each of the flow variables approximated by the interpolation functions. The flow variables within the solution domain were approximated using Lagrange finite elements of different orders. When the approximate field variables are inserted into the governing equations, residual R is obtained and the weighted average of R is forced to be zero over the computational domain as

$$\int_\Omega w_k R\mathrm{d}v = 0, \tag{32}$$

where w_k is the weight function selected from the same set of functions as of the trial functions. The residuals for each of the conservation equations were evaluated by substituting the approximations into the mass, momentum and the energy equations in the fluid and solid domains. An unstructured mesh is utilized for the fluid domain. The Arbitrary Lagrangian–Eulerian (ALE) is employed for the moving grid system of the deflection of the fin coupled to the fluid domain.

Convergence study was performed using the numerical solutions on the highest refined mesh. This is due to the fact that the exact solution of the non-linear PDEs is not available. This standard approach treats the custom mesh as a reference mesh. The reference mesh consists of 81379 domain elements and 1012 boundary elements. The reference mesh is a mesh sequence input manually by the user. This custom mesh yields a slow convergence. The reason for the slow convergence is large number of mesh nodes that are established by a very small set of gridblocks. The convergence plot shows the reciprocal of the time step size as depicted in Fig. 2. The reciprocal is divided by the time step size. The bigger the steps, the smaller the value. The oscillation time step above 400 occurs due to automatic time stepping and periodic type time dependent of the fin movement. The time dependent solver above has the flexibility to increase or decrease the time step size as it sees fit. Here, it increases the step size which indicates the solver converges successfully. In this case, the solution converged after a 6-h running on a 1.99 GHz Intel processor.

Table 2 Comparison of calculated $\overline{Nu}$ for horizontal composite system case at $Da = 10^{-5}$ and $\epsilon = 0.7$.

Ra	S	[32]	[11]	Present
10^4	0.3	1.061	1.063	1.067
10^4	0.5	1.548	1.550	1.559
10^5	0.3	2.190	2.191	2.201
10^5	0.5	3.376	3.377	3.383
10^6	0.3	5.432	5.432	5.466
10^6	0.5	6.950	6.949	7.042

Tracking the optimal number of domain elements and boundary elements are necessary to cut computation time. To achieve the optimal mesh, some tests were conducted on the predefined mesh sizes: normal, fine, finer, extra fine and extremely fine. For this, the fin oscillation at point $(x = 0.15, y = 0.8)$ with $L = 0.2$, $E = 10^9$, $A = 0.1$, $Da = 10^{-3}$, $Ra = 10^7$, $S = 0.7$ and $t_p = 0.5$ was considered. Differences between the obtained value and the reference value were given as $|\text{Error}|_{t=0.01}$ and $|\text{Error}|_{t=1.1}$. The results in Table 1 are found to be consistent by refining the mesh sizes, and a good agreement with the reference solution is obtained, where about 0.01% difference is observed for the extremely fine mesh. This suggests the selection of the extremely fine mesh.

For validation, a comparison of the streamlines and isotherms was made against that of Beckermann et al. [2] for the absence of fin in the case $\text{Ra} = 3.028 \times 10^7$, $\text{Da} = 1.296 \times 10^5$, $\text{Pr} = 6.97$, $\text{R}_\text{k} = 1.383$ and $S = 0.5$ (see Fig. 3). In addition, Table 2 exhibits a validation by calculating the values of $\overline{Nu}$ for several values of Ra and S for a horizontal composite system at $Da = 10^{-5}$ and $\epsilon = 0.7$. The small discrepancies observed in Table 2 are still within the acceptable standard. In order to validate the FSI aspect of the work, comparison was performed against Ghalambaz et al. [15], who investigated the mixed convection inside a square enclosure with no porous layer part for $t = 1.375$, $Ra = 10^6$,

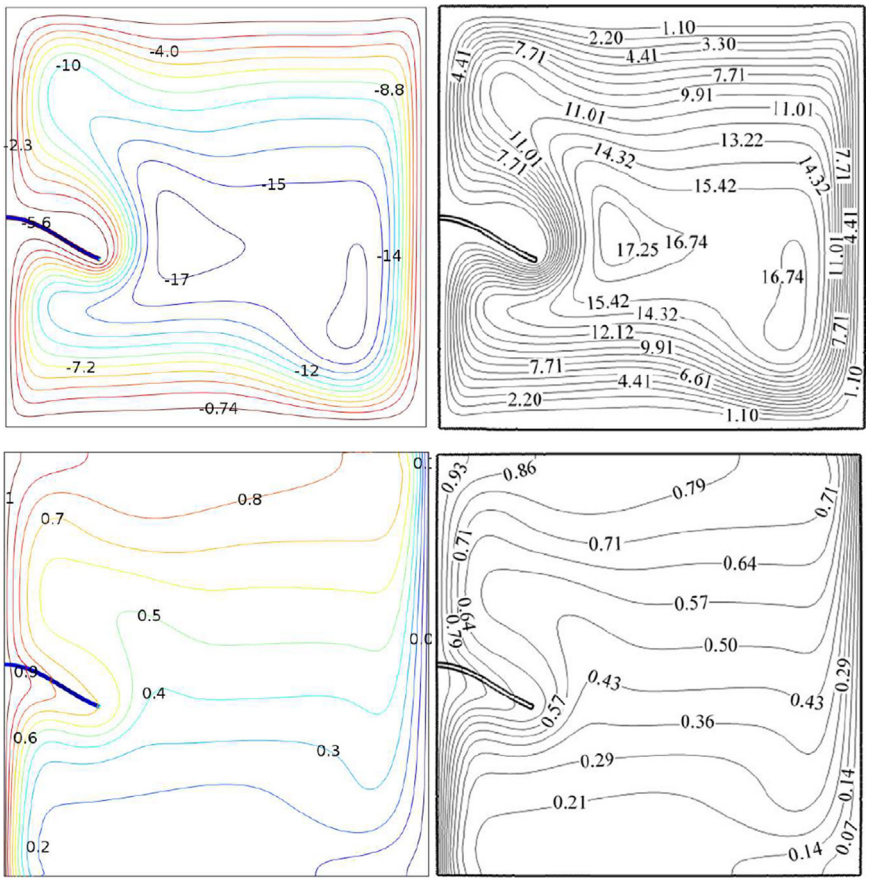

Fig. 4 A comparison of our calculated results with the previous work of Ghalambaz in the form of streamlines and isotherms; the outcomes of present work (left) and the outcomes of Ghalambaz et al. [15] (right) when $S = 1.0$, $t = 1.375$, $Ra = 10^6$, $A = 0.1$, $\text{t}_\text{p} = 0.5$ $S = 1.0, t = 1.375, Ra = 10^6, A = 0.1, t_p = 0.5$ and $E = 10^{11}$.

Table 3 Comparison of calculated $\overline{Nu}$ for special case $S = 1.0$ at $Da = 0.01$ and $Pr = 1.0$.

Ra	ϵ	[26] (FEM)	[30] (LBM)	[31] (LBM)	Present (FEM)
10^4	0.3	1.408	1.362	1.372	1.402
10^4	0.6	1.530	1.493	1.502	1.527
10^4	0.9	1.640	1.633	1.640	1.640
10^5	0.3	2.983	2.992	3.006	2.986
10^5	0.6	3.555	3.433	3.445	3.550
10^5	0.9	3.910	3.902	3.910	3.908

$A = 0.1$, $t_p = 0.5$ and $E = 10^{11}$ (cf. Fig. 4). The present results and that of previous authors' compare favourably.

An additional validation is performed through a comparison with the published work of Nithiarasu et al. [26], Seta et al. [30] and Haghshenas et al. [31] who studied a natural convection inside an enclosure filled with a porous medium for the case $Da = 0.01$ and $Pr = 1.0$. Table 3 summarizes the average Nusselt numbers for several values of the Rayleigh number and porosity parameter. Our results compare favourably with the previous results and this reaffirms the accuracy and robustness of the current computations.

4. Results and discussion

The simulation results of the present work are done for the case $\epsilon = 0.7, R_k = 2.0$ and $k_r = 10.0$. The range of the non-dimensional parameters is selected as follows: Young's Modulus $(5 \times 10^8 \leqslant E \leqslant 5 \times 10^9)$, the amplitude oscillation $(0.0 \leqslant A \leqslant 0.1)$, the period oscillation $(0.1 \leqslant t_p \leqslant 0.7)$, the fluid layer thickness $(0.5 \leqslant S \leqslant 0.9)$ and Darcy's number, $10^{-5} \leqslant Da \leqslant 10^{-2}$. The chosen range of Darcy number is based on the fact that the present model adopts the Brinkman-Forchheimer model. A Darcy number less than 10^{-5} leads to a Darcy model that is only valid for slow, viscous flow. The considered range of the Rayleigh number signifies the flow of the laminar heat transfer, and considering the Boussinesq model, the Rayleigh number is valid for the temperature difference between 294 and 324 K. The values of the Young's Modulus and amplitude oscillation correspond to a specific material that can be forced to a constant movement, such as a piezoelectric material which oscillates according to a 0.1–10 Watt source.

Fig. 5 depicts the one cycle of the flexible fin and the nearby moving mesh when $S = 0.7$, $E = 10^9$, $A = 0.1$, $Da = 10^{-5}$, $Ra = 10^7$ $K_r = 10$ and $t_p = 0.5$. This figure shows a zoomed view of the flexible fin and nearby meshes to demonstrate the moving mesh motion and deformation of the fin clearly. Each time step is depicted as subplots (a)-(h). The subplots (a) and (e) are similar as the figure is plotted for a complete cycle. A horizontal-symmetrical mesh shape can be observed for the meshes (see subplots (d) and (f), (c) and (g), and (b) and (h)). As the tip of the fin follows a dictated displacement, the sequential subplots display similar tip positions; however, the

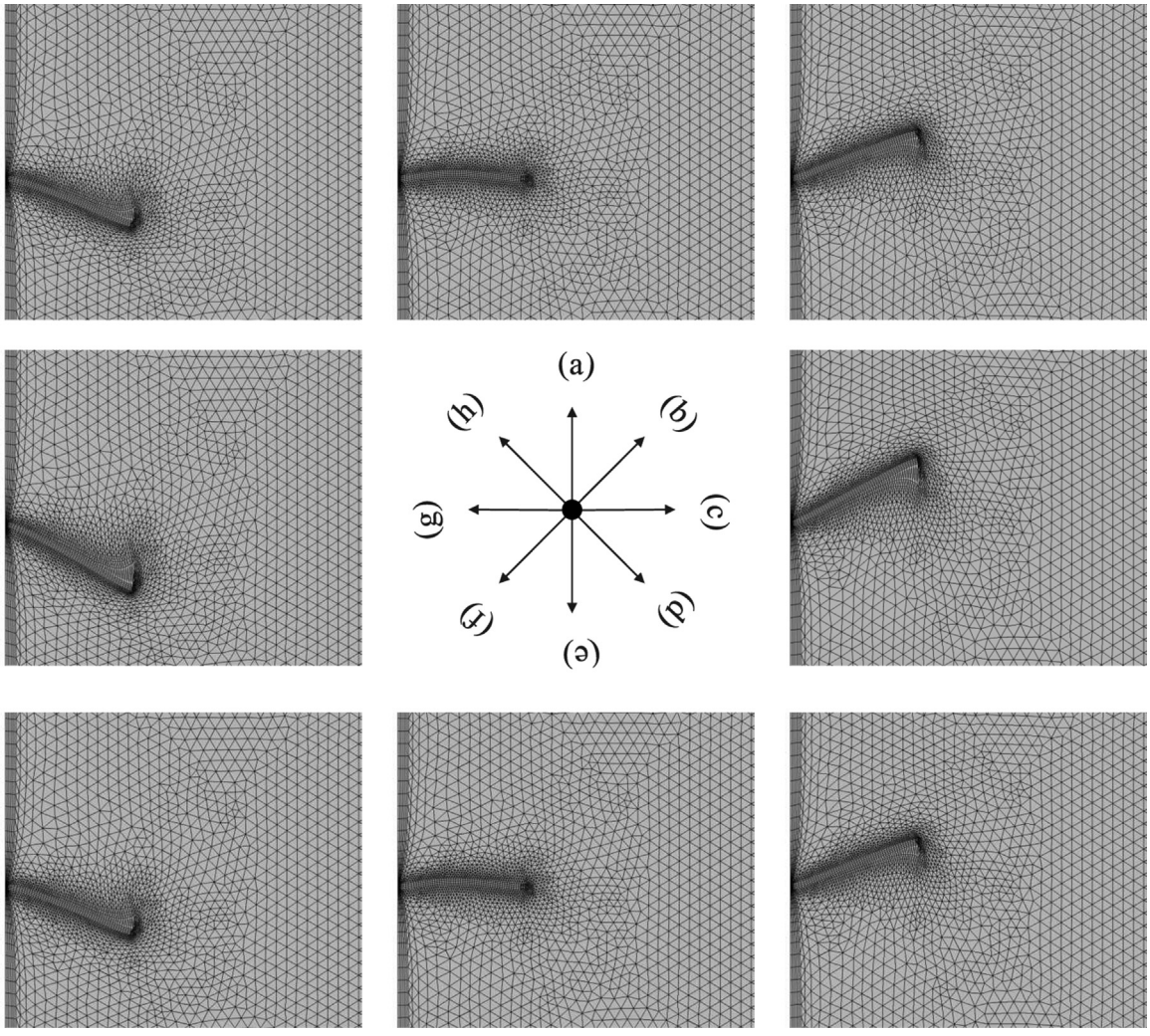

Fig. 5 One cycle time history of the flexible fin and the moving mesh after semi-steady condition when $S = 0.7$, $E = 10^9$, $A = 0.1$, $Da = 10^{-5}$ $Ra = 10^7$ $Kr = 10$ and $t_p = 0.5$.

general deformation of the fin can be different due to the interaction with the fluid.

Fig. 6 displays the dynamic streamlines for $S=0.7$, $L=0.2$, $E=10^9$, $A=0.1$, $Da=10^{-5}$, $Ra=10^7$ and $t_p=0.5$. Initially at $t=10^{-4}$ the clear fluid temperature near the how wall rises, and the gravitational force contributes to a weak flow above and below the flexible fin. Then at $t=10^{-3}$, this movement creates a clockwise circulation with two inner vortices at the clear fluid layer. The first inner vortex locates in the center while the second vortex locates in the upper part of the enclosure. The intensity of the first vortex is stronger than the second vortex. Later, the intensity of the first vortex is weaker than the second vortex, and their locations are also corrected. Denser streamlines are observed at $t=10^{-2.14}$, and the intensity of the first vortex is returned stronger than the second vortex. The fluid penetration into the porous layer is notable at $t=10^{-1.64}$. The fin tip achieves its maximum upper bending at $t=1.125$, and the first inner vortex separates into a double eye vertical formation. Later the double eye merge and the second vortex shape shrink. After a long duration, $t=1.375$, the flexible fin achieves its maximum lower bending with the shape of the first vortex elongated horizontally. Here, the flow circulation in the

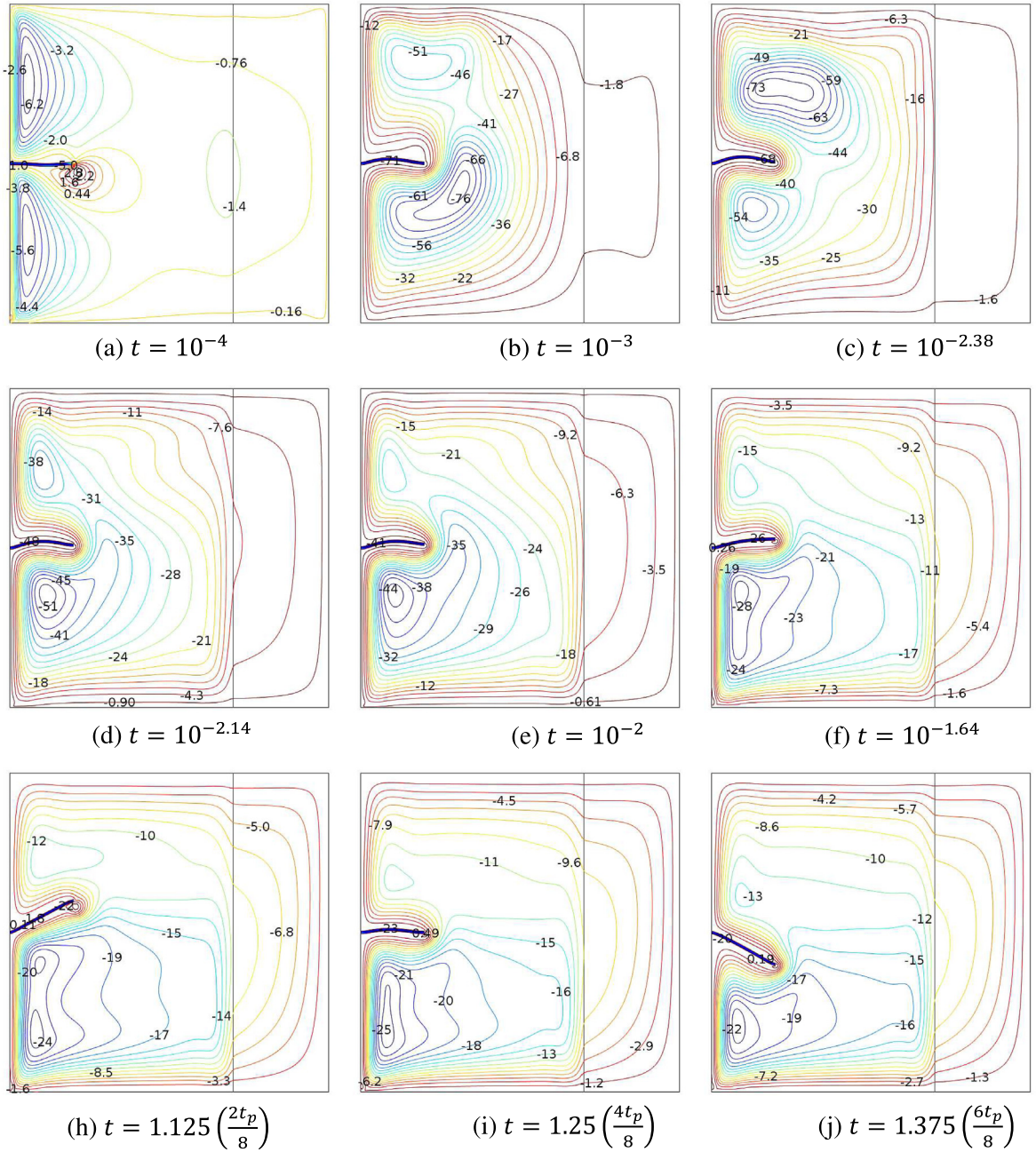

Fig. 6 The streamlines during a cycle at $S=0.7$, $L=0.2$, $E=10^9$, $A=0.1$, $Da=10^{-5}$, $Ra=10^7$ $k_r=0.1$ and $t_p=0.5$.

porous layer is strengthened. It notes that the fin oscillation impacts the area below the fin rather than above, center, or right parts of the enclosure. This due to the fluid motion of the gravitational force is downward, and hence, the influence of the fin oscillation gathers at lower areas of the enclosure which are below the fin.

Fig. 7 exhibits the transient evolution of the isotherms for $S = 0.7$, $L = 0.2$, $E = 10^9$, $A = 0.1$, $\mathrm{Da} = 10^{-5}$, $\mathrm{Ra} = 10^7$, $\mathrm{k_r} = 10$ and $t_p = 0.5$. The isotherms at $t = 10^{-4}$ and $t = 10^{-3}$ are parallel to the vertical wall, in particular at the porous layer. This indicates that the conduction heat transfer mechanism is dominant in the system. The heat from the clear fluid region reaches the porous region which results in a slight distortion and little perturbed isotherm around the fin extend to the middle. Then at $t = 10^{-2.14}$, the isotherms evolve and distribute in the whole enclosure. It appears from the figures that later at $t = 10^{-2}$, the global flow and isotherm patterns are fixed where the boomerang shape is created around the fin. At $t = 10^{-1.64}$, the fin tip is moving upward, but no substantial change in the isotherms can be observed. The fin tip achieves its maximum upper bending at $t = 1.125$, and the boomerang shape is disappeared. Later, the boomerang shape is returned at $t = 1.25$,

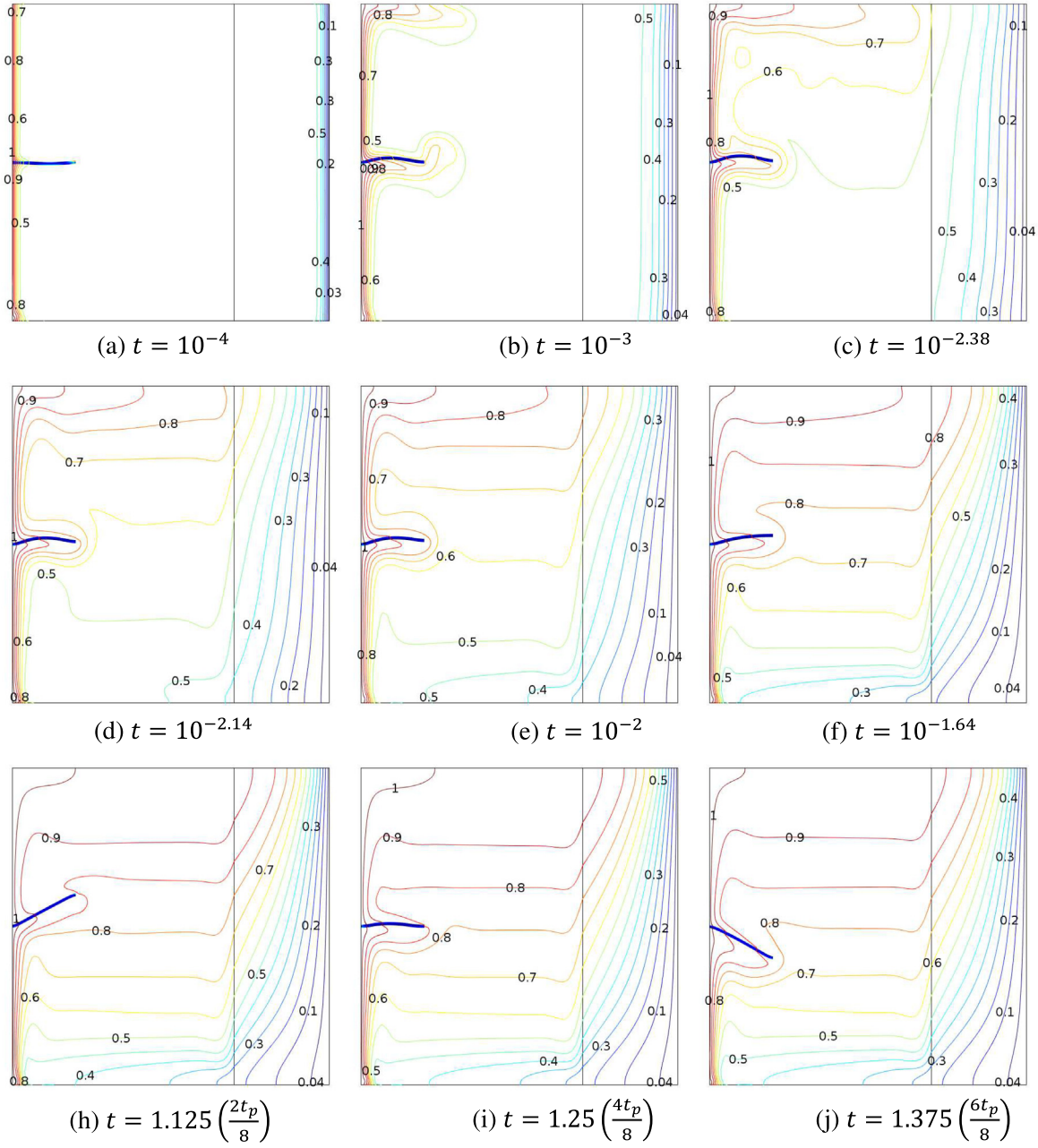

Fig. 7 Time evolution of the isotherms at $S = 0.7$, $L = 0.2$, $E = 10^9$, $A = 0.1$, $Da = 10^{-5}$, $Ra = 10^7$, $\mathrm{K_r} = 10$ and $t_p = 0.5$.

and it pushed downward as the fin deflection reach its maximum lower bending at $t = 1.375$. The isotherms are aligned in a mostly horizontal manner in clear fluid layer while the isotherms are aligned in a mostly vertical manner in the porous layer. The isotherm patterns are aligned horizontally, indicating that the heavy-cold fluid leading the fluid circulation, and the cold denser fluid in the clear region is pushed down. On the other hand, the isotherms in the porous layer are aligned vertically, giving evidence of that heat is transferred almost entirely by pure conduction via direct molecular collision.

Fig. 8 shows the effects of the fluid layer thickness on the streamlines for several values of the Darcy number for the case $L = 0.2$, $Da = 10^{-5}$, $E = 10^{9}$, $t_p = 0.5$, $Ra = 10_7$ and $t = 1.375$. The changing of the semi-steady flow motion as the clear fluid thickness varies is seen in Fig. 8(a). As the Darcy number increases (from the left to the right), the flow circulation strength increases and this eventually breaks up the vortex. The vortex occupies the zone below the flexible fin at $Da = 10^{-4}, 10^{-3}$ while at $Da = 10^{-2}$, the left vortex occupies the zone above the flexible fin and the right vortex appears

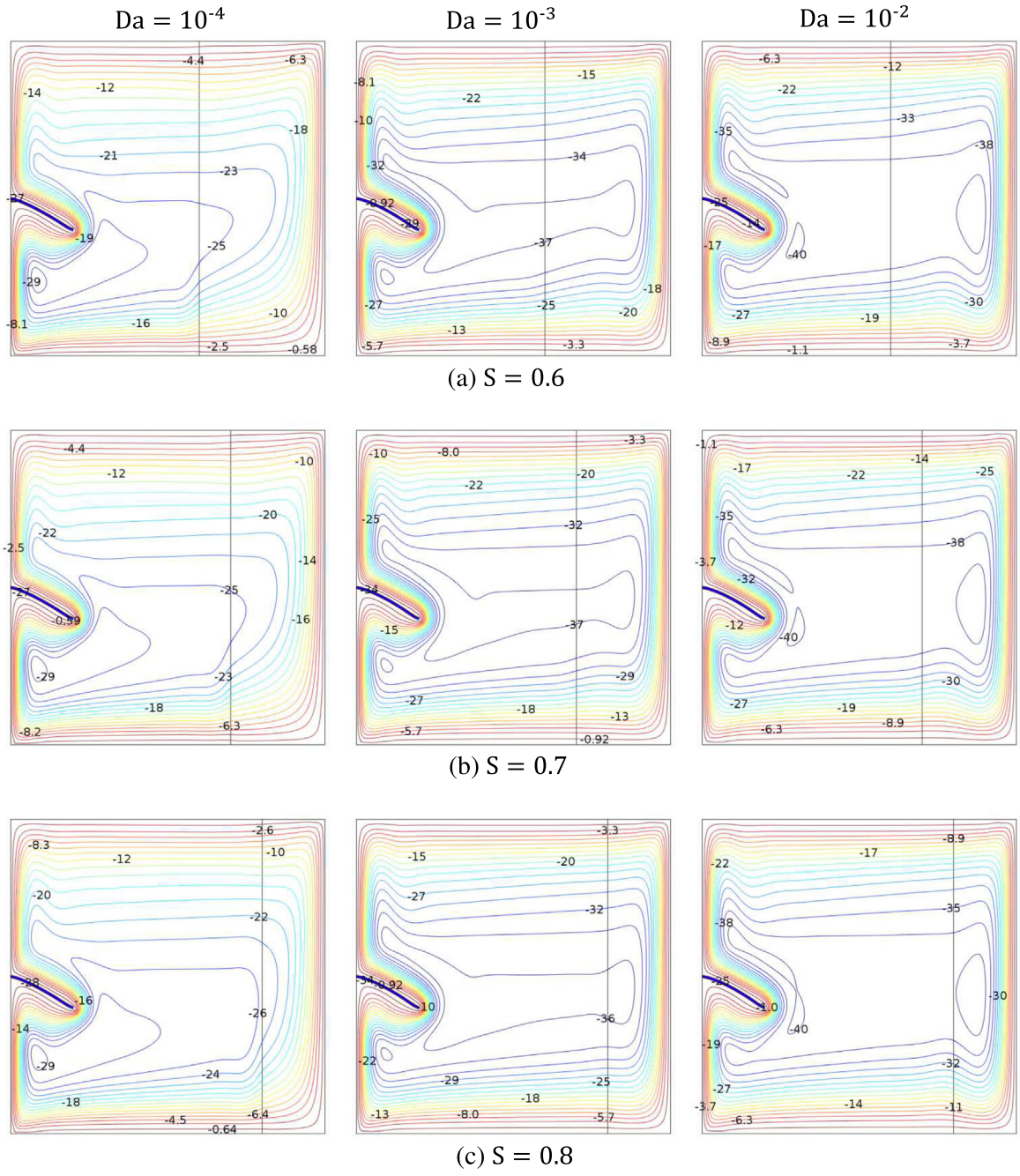

Fig. 8 Streamlines for different Darcy number and S at $L = 0.2$, $Da = 10^{-5}$ $E = 10^{9}$ $A = 0.1$, $Ra = 10^{7}$, $t_p = 0.5$ and $t = 1.375$.

close to the right cold wall. This is due to the porous layer which acts almost like a solid at a relatively small Darcy number. The fluid circulation is almost unaffected by the porous layer thickness. The flow can be seen penetrating into the porous medium completely and the convective flow is deviated slightly.

Variations of the local Nusselt number against the amplitude for two cycles are shown in Fig. 9 for the case $L = 0.2$,

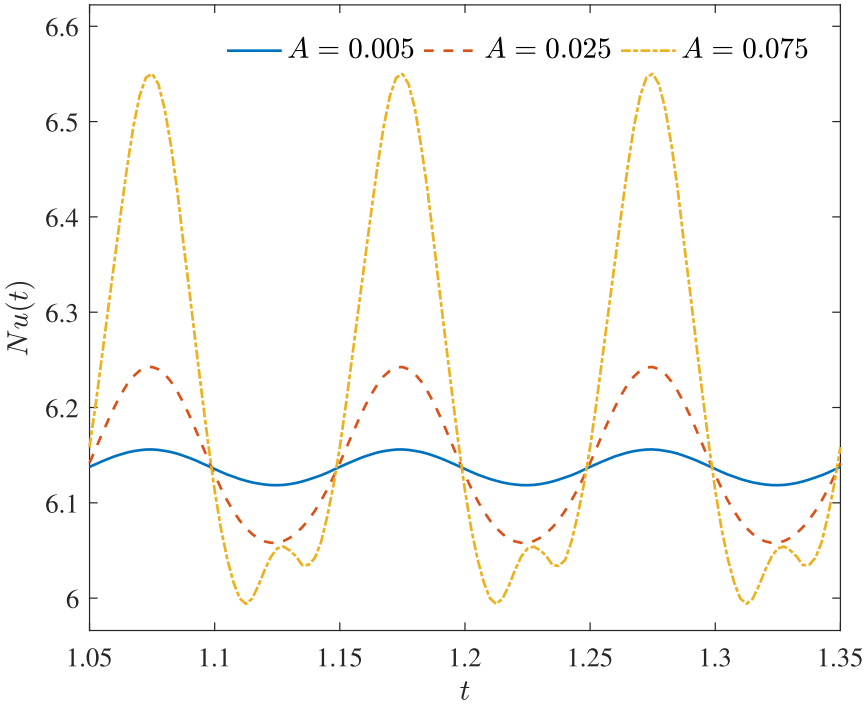

Fig. 9 Effects of the amplitude of the fin oscillation on the local Nusselt number for $L = 0.2$, $Da = 10^{-5}$, $E = 10^9$, $Ra = 10^7$ $K_r = 10$, $t_p = 0.1$ and $S = 0.7$.

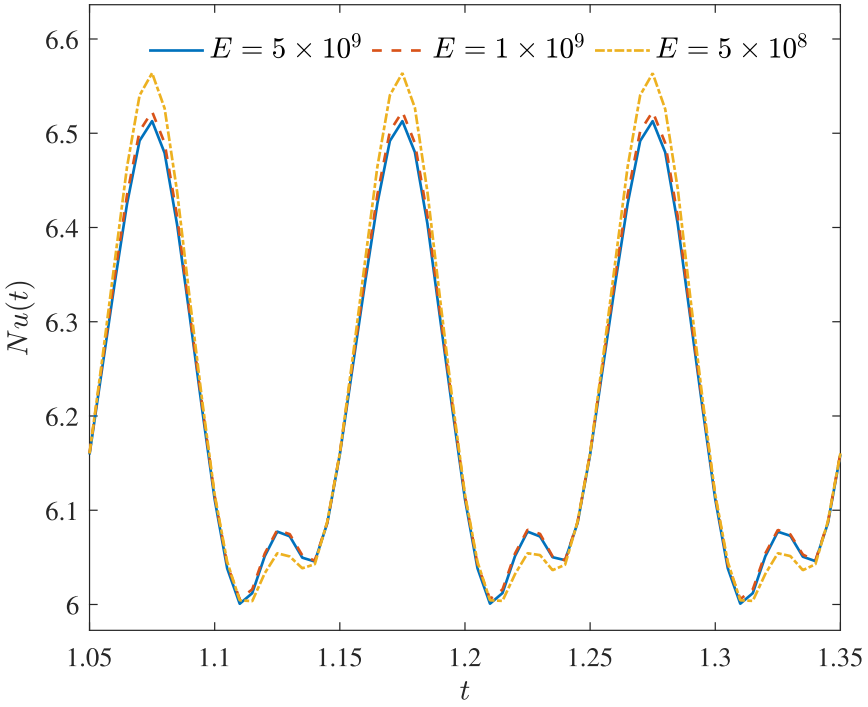

Fig. 10 Effects of the Young's Modulus on the local Nusselt number for $L = 0.2$, $Da = 10^{-5}$, $A = 0.075$, $Ra = 10^7$, $K_r = 10$, $t_p = 0.1$ and $S = 0.7$.

$Da = 10^{-5}$, $E = 10^9$, $Ra = 10^7$, $K_r = 10$, $t_p = 0.1$ and $S = 0.7$. The transient Nusselt number oscillates with periodic variation of the fin tip position for all amplitudes considered in this study. Perfectly sinusoidal laws were found for all small-amplitude values. When the oscillation amplitudes are large, the motion of the fin sips a massive amount of fluid, which results in a significant amount of the momentum exchange between the fluid in the vicinity of the hot wall and the fin. The tip spot oscilla-

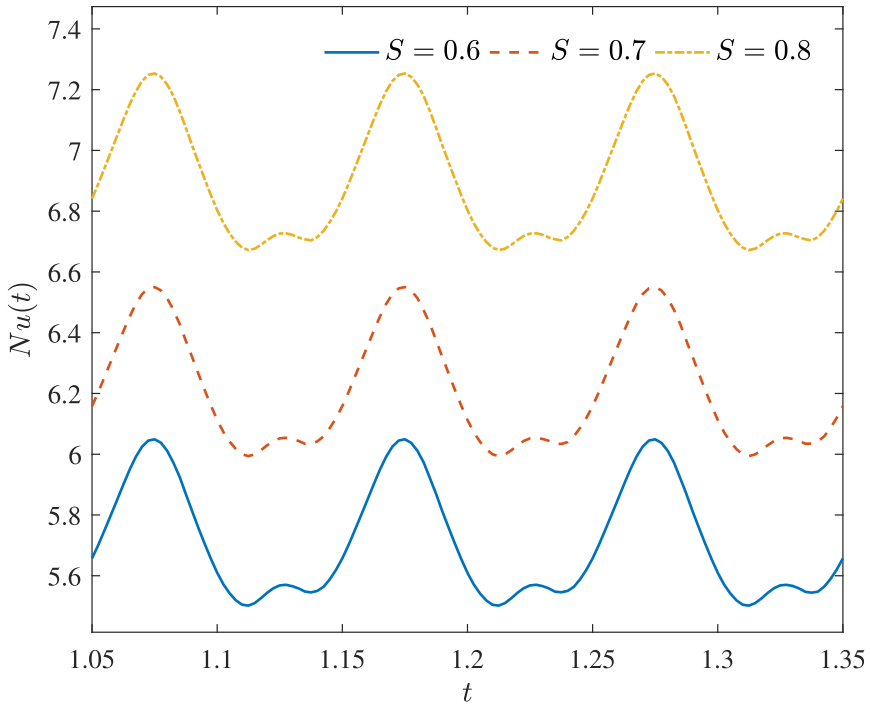

Fig. 11 Effects of the fluid layer thickness on the instaneous Nusselt number for $L = 0.2$, Da $= 10^{-5}$, $A = 0.075$, $Ra = 10^7$, $t_p = 0.1$ and $E = 10^9$.

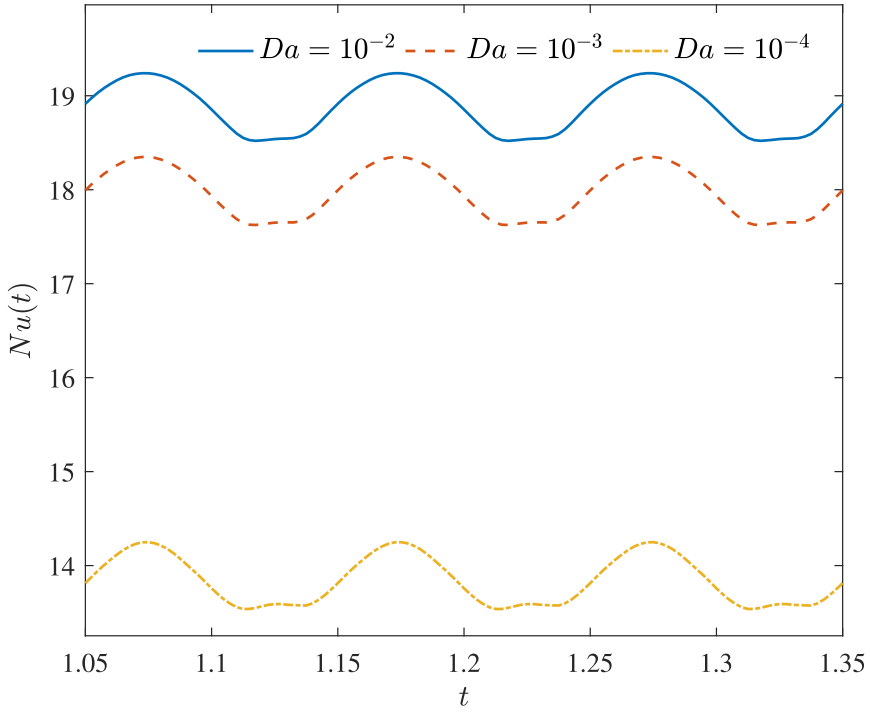

Fig. 12 Effects of the Darcy number on the local Nusselt number for $L = 0.2, A = 0.075, Ra = 10^7, t_p = 0.1$ and $E = 10^9$.

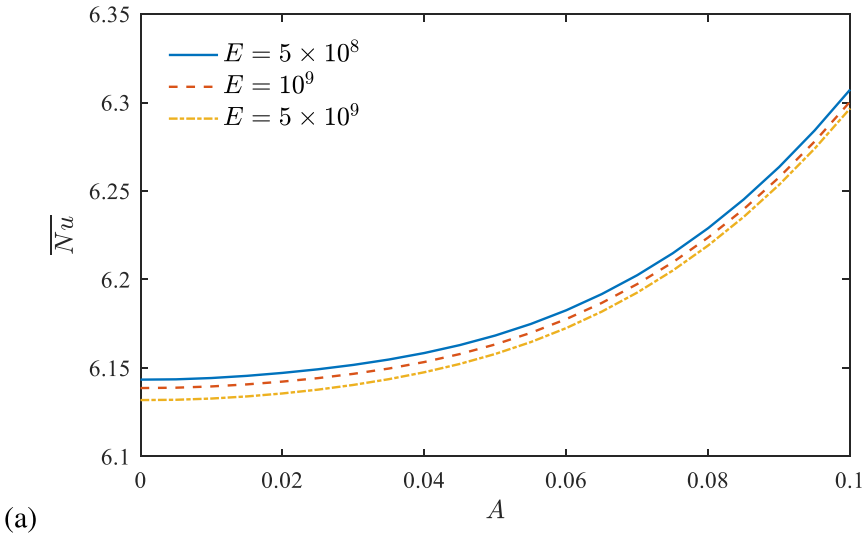

(a)

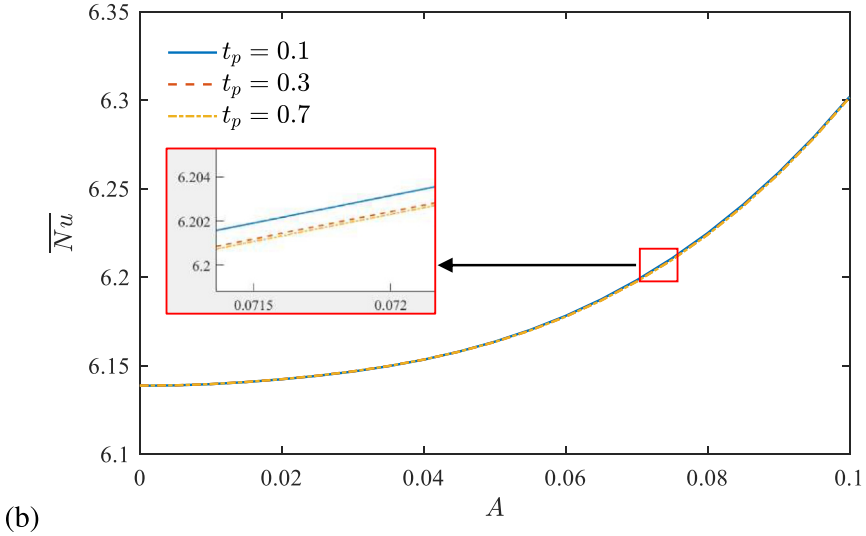

(b)

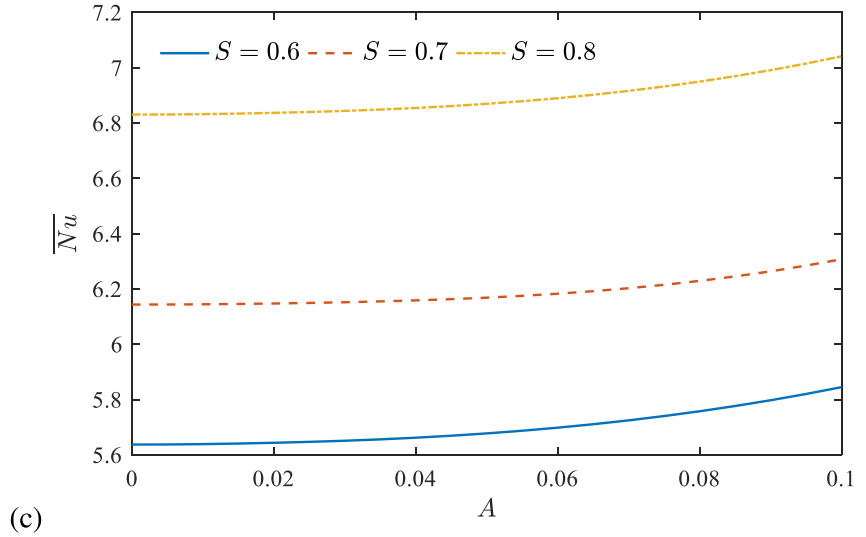

(c)

Fig. 13 Effects of the value of Young's Modulus (a), oscillation period (b), and fluid layer thickness (c) on the average Nusselt number against the oscillation-amplitude when $L = 0.2$ and $Ra = 10^7$.

tion with large amplitude ($A = 0.075$) causes a relatively large amplification of the momentum exchange; therefore, the instantaneous of the flow disagree to a high degree from the weak-oscillating case. The flow amplification brings the amount of increase of Nu when the fin moves downward. The lower position of the flexible part assists the convective flow to absorb the heat from the hot source better.

Fig. 10 exhibits the effects of Young's Modulus on the instantaneous Nusselt number for $L = 0.2$, $Da = 10^{-5}$, $A = 0.075$, $Ra = 10^7$, $k_r = 10$, $t_p = 0.1$ and $S = 0.7$. The transient heat transfer profiles for $E = 5 \times 10^9$ and $E = 1 \times 10^9$ are almost matching point by point. This due to the dictated fin deflection, which is independent from the fluid interaction effect so that the instaneous heat transfer rate remain unchanged by increasing E value. In contrast, different condition occurs when E value is relative low. The shape of flexible fin modifies the total maximum Nusselt number and the local maximum Nusselt number. he reason behind this situation is the deformation of the fin due to the interaction with the fluid flow.

Fig. 11 depicts the influence of fluid layer thickness on the local Nusselt number for $L = 0.2$, $Da = 10^{-5}$, $A = 0.075$, $Ra = 10^7$, $t_p = 0.1$ and $E = 10^9$. The larger clear fluid layer thickness the higher instantaneous Nusselt number at all tip position. The cold fluid departs from the left upper part of the enclosure and arrives at the right wall. The cold fluid starts to dispose of heat from the left wall and agitate again. In this process, the fluid circulation strength is accelerated then the overall thermal performance at the hot wall increases. There are some local apexes for the heat transfer rate which are the result of the sequence of events. The variation of the size of the fluid layer does not affect the fluid area circulation, but the partition reduces the free space for fluid to move from the hot wall to the cold wall when the porous layer thickness increases. The impermeable partition does not allow fluid to pass through it. The impact of the partition/interface to the fluid circulation would be given in the next figure.

Fig. 12 displays the influence of Darcy number on the instantaneous Nusselt number $L = 0.2$, $A = 0.075$, $Ra = 10^7$, $t_p = 0.1$ and $E = 10^9$. The stronger the Darcy number the higher the instantaneous Nusselt number at all tip positions. This happens due to the Darcy number as it represents the relative effect of the permeability of the medium. When the permeability increases, a significant amount of fluid enters the porous layer, and the porous layer no longer acts as a hydrodynamic barrier to the fluid movements.

Fig. 13 shows the influence of the value of Young's modulus (a), oscillation period (b) and fluid layer thickness (c) on the average Nusselt number as a function of the amplitude of the oscillation when $L = 0.2$ and $Ra = 10^7$. The larger oscillation amplitude the higher average Nusselt number at the considered stiffness, oscillation period and fluid layer thickness. When the oscillation-amplitude increases, the flow movement is intense and boosts the heat transfer. Fig. 13(a) shows that when the fin is very flexible, $E = 5 \times 10^8$, the greatest improvement of the overall heat transfer rate can be seen. This is since the fluid–structure interaction can work well to deflect the fin for a very elastic fin. However, when the amplitude oscillation gets more substantial, the influence of the value of Young's modulus weakens. It seems that the total Nusselt number is fixed by changing the period oscillation, as shown in Fig. 13(b). Increasing the period or decreasing the frequency reduces the rate of heat transfer slightly.The increase of the oscillation amplitude from zero to 0.1 could improve the average Nusselt number from about 6.14 to 6.35, which shows about 3.4 percent improvement, i.e., 100x(6.35–6.14)/6.14.

5. Conclusions

In the present work, the impact of fin elasticity and the fluid layer thickness on the flow and temperature distribution as well as the heat transfer rate was investigated. The Arbitrary Lagrangian–Eulerian (ALE) in a moving mesh system was utilized to couple the large deformations of the fin with the fluid domain. The numerical simulations were done using COMSOL software. The followings are the main findings:

1. The fin oscillation impacts the area below the fin rather than the area above the fin or the area in the center. The position of the fin tip modifies the number and location of the core of the flow circulation.
2. There are some local apexes for the heat transfer rate, which are the result of the sequence of events. The shape of flexible fin modifies the global maximum of the transient Nusselt number and the local maximum of the transient Nusselt number.
3. The overall rate of heat transfer increases exponentially with the rise of the oscillation amplitude.
4. The overall heat transfer rate is enhanced by increasing the Darcy number, the fluid layer thickness and the fin elasticity. The variation of the heat transfer enhancement is almost independent of the period.

Declaration of Competing Interest

The authors declare that there is no conflict of interests regarding the publication of this article.

Acknowledgment

The financial support received from the Malaysian Ministry of Education under the research grant FRGS/1/2019/STG06/UKM/01/2 is gratefully acknowledged.

References

[1] A. Tahmasebi, M. Mahdavi, M. Ghalambaz, Local thermal nonequilibrium conjugate natural convection heat transfer of nanofluids in a cavity partially filled with porous media using Buongiorno's model, Numer. Heat Transf. Part A 73 (2018) 254–276.

[2] C. Beckermann, S. Ramdhyani, R. Viskanta, Natural convection flow and heat transfer between fluid layer and porous layer inside a rectangular enclosure, J. Heat Transf. 109 (1987) 363–371.

[3] C. Beckermann, S. Ramdhyani, R. Viskanta, Natural convection in vertical enclosures containing simultaneously fluid and porous layer, J. Fluid Mech. 186 (1988) 257–284.

[4] Z. Du, E. Bilgen, natural convection in vertical cavities with partially filled heat-generating porous media, Numer. Heat Transf. Part A 18 (1990) 371–386.

[5] M. Song, R. Viskanta, Natural convection flow and heat transfer within a rectangular enclosure containing a vertical porous layer, Int. J. Heat Mass Transf. 37 (1994) 2425–2438.
[6] F. Chen, C. Chen, Convection in superposed fluid and porous layer, J. Fluid Mech. 234 (1992) 97–119.
[7] B. Goyeau, D. Lhuillier, D. Gobin, M. Velarde, Momentum transport at a fluid-porous interface, Int. J. Heat Mass Transf. 46 (2003) 4071–4081.
[8] X. Chen, P. Yu, Y. Sui, S. Winoto, H. Low, Natural convection in a cavity filled with porous layers on the top and bottom walls, Transp. Porous Med. 78 (2009) 259–276.
[9] M.A. Ismael, A.J. Chamkha, Conjugate natural convection in a differentially heated composite enclosure filled with a nanofluid, J. Porous Media 18 (2015) 699–716.
[10] A. Baytas, A. Baytas, Thermal non-equilibrium natural convection in a square enclosure with heat-generating porous layer on inner walls, Transp. Porous Med. 120 (2017) 167–182.
[11] A. Alsabery, A. Chamkha, H. Saleh, I. Hashim, Natural convection flow of a nanofluid in an inclined square enclosure partially filled with a porous medium, Sci. Rep. 7 (2017) 2357, art. no. 2357.
[12] M. Sheikholeslami, M. Sheremet, A. Shafee, I. Tlili, Simulation of nanoliquid thermogravitational convection within a porous chamber imposing magnetic and radiation impacts, Physica A: Stat. Mech. Appl. 550 (2020), art. no. 124058.
[13] B. Alshuraiaan, K. Khanafer, The effect of the position of the heated thin porous fin on the laminar natural convection heat transfer in a differentially heated cavity, Int. Comm. Heat Mass Transf. 78 (2016) 190–199.
[14] M. Sheikholeslami, R. Haq, A. Shafee, Z. Li, Heat transfer behavior of nanoparticle enhanced PCM solidification through an enclosure with V shaped fins, Int. J. Heat Mass Transf. 130 (2019) 1322–1342.
[15] M. Ghalambaz, E. Jamesahar, M. Ismael, A. Chamkha, Fluid-structure interaction study of natural convection heat transfer over a flexible oscillating fin in a square cavity, Int. J. Thermal Sci. 111 (2017) 256–273.
[16] K. Khanafer, Fluid-structure interaction analysis of non-Darcian effects on natural convection in a porous enclosure, Int. J. Heat Mass Transf. 58 (2013) 382–394.
[17] K. Khanafer, Comparison of flow and heat transfer characteristics in a lid-driven cavity between flexible and modified geometry of a heated bottom wall, Int. J. Heat Mass Transf. 78 (2014) 1032–1041.
[18] F. Selimefendigil, H. Oztop, Analysis of MHD mixed convection in a flexible walled and nanofluids filled lid-driven cavity with volumetric heat generation, Int. J. Mech. Sci. 118 (2016) 113–124.
[19] F. Selimefendigil, H. Oztop, Mixed convection in a partially heated triangular cavity filled with nanofluid having a partially flexible wall and internal heat generation, J. Taiwan Inst. Chem. Eng. 70 (2017) 168–178.
[20] A. Raisi, I. Arvin, A numerical study of the effect of fluid-structure interaction on transient natural convection in an air-filled square cavity, Int. J. Therm. Sci. 128 (2018) 1–14.
[21] A. Alsabery, M. Sheremet, M. Ghalambaz, A. Chamkha, I. Hashim, Fluid-structure interaction in natural convection heat transfer in an oblique cavity with a flexible oscillating fin and partial heating, Appl. Therm. Eng. 145 (2018) 80–97.
[22] A. Alsabery, H. Saleh, M. Ghalambaz, A. Chamkha, I. Hashim, Fluid-structure interaction analysis of transient convection heat transfer in a cavity containing inner solid cylinder and flexible right wall, Int. J. Numer. Meth. Heat Fluid Flow 29 (2019) 3756–3780.
[23] M. Ghalandari, S. Bornassi, S. Shamshirband, A. Mosavi, K. Chau, Investigation of submerged structures' flexibility on sloshing frequency using a boundary element method and finite element analysis, Eng. Appl. Comput. Fluid Mech. 13 (2019) 519–528.
[24] I. Mahariq, M. Kavyanpoor, M. Ghalandari, M. Nazari, D. Bui, Identification of nonlinear model for rotary high aspect ratio flexible blade using free vibration response, Alexandria Eng. J. 59 (4) (2020) 2131–2139, https://doi.org/10.1016/j.aej.2020.01.029.
[25] D.D. Gray, A. Giorgini, The validity of the boussinesq approximation for liquids and gases, Int. J. Heat Mass Transf. 19 (1976) 545–551.
[26] P. Nithiarasu, K. Seetharamu, T. Sundararajan, Natural convective heat transfer in an enclosure filled with fluid saturated variable porosity medium, Int. J. Heat Mass Transf. 40 (1997) 3955–3967.
[27] I. Mahariq, H. Tarman, M. Kuzuoğlu, On the accuracy of spectral element method in electromagnetic scattering problems, Int. J. Comput. Theory Eng. 6 (2014) 495–499.
[28] I. Mahariq, On the application of the spectral element method in electromagnetic problems involving domain decomposition, Turkish J. Elect. Eng. Comput. Sci. 25 (2017) 1059–1069.
[29] I. Mahariq, A. Erciyas, A spectral element method for the solution of magnetostatic fields, Turkish J. Elect. Eng. Comput. Sci. 25 (2017) 2922–2932.
[30] T. Seta, E. Takegoshi, K. Okui, Lattice Boltzmann simulation of natural convection in porous media, Math. Comput. Simulat. 72 (2006) 195–200.
[31] A. Haghshenas, M. Nasr, M. Rahimian, Numerical simulation of natural convection in an open-ended square cavity filled with porous medium by lattice Boltzmann method, Int. Comm. Heat Mass Transf. 37 (2010) 1513–1519.
[32] A. Singh, G. Thorpe, natural convection in a confined fluid overlying a porous layer-a comparison, Indian J. Pure Appl. Math 26 (1995) 81–95.